Proceedings of the Czech–Japanese Seminar in Applied Mathematics 2006
Czech Technical University in Prague, September 14-17, 2006
pp. 114–136

QUANTITATIVE STUDY OF ADAPTIVE MESH FEM WITH LOCALIZATION INDEX OF PATTERNS

MASATO KIMURA[1], HIDEKI KOMURA[2], MASAYASU MIMURA[3],
HIDENORI MIYOSHI[2], TAKESHI TAKAISHI[4], AND DAISHIN UEYAMA[3]

Abstract. We study the effectivity of an adaptive mesh algorithm with triangular finite elements for two or three dimensional pattern dynamics appearing in several reaction-diffusion systems. The aim of this paper is to investigate a relation between the effectivity of the adaptive mesh and the pattern profile through several numerical experiments. Based on the result of our previous paper [6], the effectivity of the adaptive mesh is estimated in terms of the compression rate of the adapted mesh. We introduce a quantity called localization index which characterizes pattern profiles of numerical solutions.

Key words. Pattern dynamics, reaction-diffusion system, finite element method, adaptive mesh.

AMS subject classifications. 35K57, 65M50, 65M60, 74S05

1. Introduction. The adaptive mesh technique is widely used in finite element simulations for various problems [1, 2, 3, 4, 11, 17, 19, 20, 27]. In particular, based on a posteriori error estimates ([25] etc.), adaptive mesh control theory has been well established for stationary problems. On the other hand, for time evolution problems, many numerical simulations have been done with dynamic adaptive mesh control algorithms, but the behavior and efficiency of mesh adaptivity do not seem to have been enough analyzed.

The adaptive mesh finite element method (FEM) has been developed in recent years for various kind of time evolution problems. Such adaptive mesh algorithm makes the finite element mesh adapt to the time dependent profile of a numerical solution automatically. This is very effective for solutions which exhibits spatiotemporal patterns, such as in reaction-diffusion systems. As important mathematical models of various spatiotemporal patterns in nonlinear nonequilibrium systems, various reaction-diffusion systems are widely proposed [8, 13, 16, 18, 22, 26]. A great variety of interesting pattern dynamics such as internal layer motion, traveling front, pulse and spot, stripe or laminar pattern, labyrinth pattern, spiral pattern, etc., produced by the reaction-diffusion systems have gained recognition as interesting research objects through a large number of numerical simulations. Recently, reaction-diffusion systems such as three dimensional problems, multi-variable systems and problems very close to singular or critical cases, have been attracting people's notice.

By the following properties (i) and/or (ii), most of such attractive spatial patterns and their temporal dynamics are characterized. (i) Spatial localization: Very small spatial scale structure, such as spatially rapid change of a variable, occurs only in

---

[1] Faculty of Mathematics, Kyushu University, Fukuoka, 812-8581, Japan

[2] Department of Mathematical and Life Sciences, Graduate School of Science, Hiroshima University, Higashi-Hiroshima, 739-8526, Japan

[3] School of Science and Technology, Meiji University, Higashimita 1-1-1, Tama-ku Kawasaki, 214-8571, Japan

[4] Department of Computer Science, Faculty of Informatics, Hiroshima Kokusai Gakuin University, Nakano 6-20-1, Aki-ku, Hiroshima, 739-0321, Japan

a moving small restricted region. (ii) Temporal localization: Some kind of patterns only appear in specific time regions as oscillatory or transitional phenomena. Another important example is the pattern formation as a self-organizational process.

In our previous paper [6], we investigated a quantitatively for the effectiveness of the adaptive mesh FEM for pattern dynamics appearing in the following reaction-diffusion systems. First one is the following reaction-diffusion system with an activator-inhibitor type nonlinearity (activator-inhibitor system) [18, 22]:

$$(1.1)\qquad (AI)\begin{cases} \varepsilon\tau\dfrac{\partial u}{\partial t} = \varepsilon^2\Delta u + u(u-a)(1-u) - v & , \ \text{in } \Omega\times(0,T), \\[2ex] \dfrac{\partial v}{\partial t} = d\Delta v + u - \lambda v & , \ \text{in } \Omega\times(0,T), \end{cases}$$

where $\varepsilon,\ \tau,\ d,\ \lambda > 0,\ 0 < a < \frac{1}{2}$ are constant values .

Another one is the reaction-diffusion system with a resource-consumer type nonlinearity, proposed as a mathematical model of an autocatalytic chemical reaction (Gray-Scott model) [8, 16].

$$(1.2)\qquad (GS)\begin{cases} \dfrac{\partial u}{\partial t} = d_u\Delta u - uv^2 + A(1-u) & , \ \text{in } \Omega\times(0,T), \\[2ex] \dfrac{\partial v}{\partial t} = d_v\Delta v + uv^2 - \alpha v & , \ \text{in } \Omega\times(0,T), \end{cases}$$

where $d_u,\ d_v,\ \alpha > 0,\ A \geq 0$ are constant values.

In both cases, Neumann boundary condition $\frac{\partial u}{\partial \nu} = \frac{\partial v}{\partial \nu} = 0$ on $\partial\Omega$ is supposed, where Ω is a bounded Lipschitz domain in $\mathbb{R}^n$ ($n = 2$ or 3). The initial condition is given by $u(x,0) = u_0(x), v(x,0) = v_0(x)$ ($x \in \Omega$). They exhibit various kind of patterns depending on parameters (see section 2 and [6]).

To measure the validity of our algorithm, we introduced a quantity called compression rate of adaptive mesh and we showed that the compression rate gives a good quantitative index instead of an intuitional judgment of the mesh adaptivity in [6].

This paper is a follow-up of [6]. The organization of this paper is as follows. A brief introduction of the result concerning the compression rate is given in the next section. Some typical adaptive mesh FEM simulations for (1.1) and (1.2) are presented. In section 3, we introduce the localization index and give several examples of typical functions with pattern. Through some numerical and analytical comparisons between the compression rate and the localization index in section 4, it is shown that the compression rate is almost proportional to the localization index. In the last section, we give a small example of applications of our adaptive mesh finite element method to pattern dynamics in reaction-diffusion systems. We remark that the contents of this paper are mainly based on the results in [7, 12]. Our numerical simulations in this research were computed mainly on a workstation system, COMPAQ AlphaStation XP1000 (Alpha21264 667MHz, 1GB Memory).

2. Compression rate of adaptive mesh FEM. If we need very accurate numerical solutions to analyze complicated and critical pattern dynamics, computing on very fine uniform mesh has limitation in the sense of computational time and memory size without use of very large computer systems. Adaptive mesh FEM enables us to use meshes of very fine scale near the spatially localized pattern and coarse meshes for the region without patterns. As the pattern changes, the adaptive mesh can track it by refinement and coarsening of the meshes. We developed a numerical code to solve general reaction-diffusion systems by using ALBERTA. ALBERTA is a C language library for adaptive mesh FEM created by A. Schmidt and K.G. Siebert [20, 21].

We use mainly very standard P_1 element (or P_2 element for some examples) on a triangular or tetrahedral mesh with backward Euler time discretization. For the nonlinear term, the values in the previous time step are used. The obtained linear system at each time step is solved by a standard preconditioned conjugate gradient solver. The adaptive mesh control library equipped in ALBERTA enables us to use the equidistributional strategy for mesh control with a bisection algorithm and an error estimator based on an a posteriori estimate. To control the accuracy of the numerical solution, we use a tolerance parameter *tol*. The smaller the parameter *tol* is, the finer triangular elements are generated to be adapted to the numerical solution. For the detail of these numerical techniques, please see the manual of the ALBERTA library [21].

All numerical simulation in this section is computed on the unit square or cubic domain $\Omega = (0,1)^n$ $(n = 2,\ 3)$.

In Fig.2.1, we show an example of adaptive mesh FEM for the activator-inhibitor system (1.1). The variables u and v represent activator and inhibitor, respectively. We choose ε sufficiently small comparing with d such that there appears the internal transition layer between two stable states in the u-component. For the initial values, $u_0(x)$ is a given step function and $v_0(x) \equiv 0$ as shown in Fig.2.1. A typical pattern dynamics with (1.1) is shown in Fig.2.1, where an internal layer of specific width and height forms in early stage, after that, it moves slowly. Starting from a fine uniform mesh, the mesh adapts to the profile of u, and the mesh changes to track the internal layer of the variable u as it moves. Since such an internal layer solution forms very sparse localized pattern, the adaptive mesh FEM works effectively as we expected.

We show other examples of adaptive mesh FEM for the Gray-Scott model (1.2). The variables u and v represent concentration of two chemical reactants, where the substance v consumes the resource substance u by an autocatalytic process. The term $A(1-u)$ corresponds to a supply of the resource substance u from a reservoir, if $A > 0$. The Gray-Scott model is known for its great variety of patterns (see [6, 10, 16] etc.).

Fig.2.2 is a typical traveling spot (spike) pattern appearing in the Gray-Scott model without resource supply ($A = 0$). The consumer (variable v) forms several traveling spots, but this is a transitional phenomenon since only finite resource is given at the initial condition; $u_0(x) = u_0$, where u_0 is a positive constant.

Starting from a fine uniform mesh, the mesh adapts to the profile of u and v at $t = 50$. The mesh changes not only to track the traveling spots of the variable v, but also the profile of u as they moves. Since such a transitional traveling spot solution is spatiotemporally localized, the adaptive mesh FEM also works effectively.

The Gray-Scott model with resource supply ($A > 0$), which is the origical model, produces several kind of densely distributed patterns ([16]). In particular, it is studied as a model of a self-replication dynamics [14, 15, 23, 24]. Fig.2.3 shows a typical self-replication process in which the spot pattern occupies the domain densely after repeating self-replication of spots. The profile of v and the adapted mesh are shown in Fig.2.3. But, when the spot pattern is distributed densely at $t = 8000$, the mesh looks almost uniformly fine

on the whole domain.

The last examples of our adaptive mesh FEM are three dimensional simulations

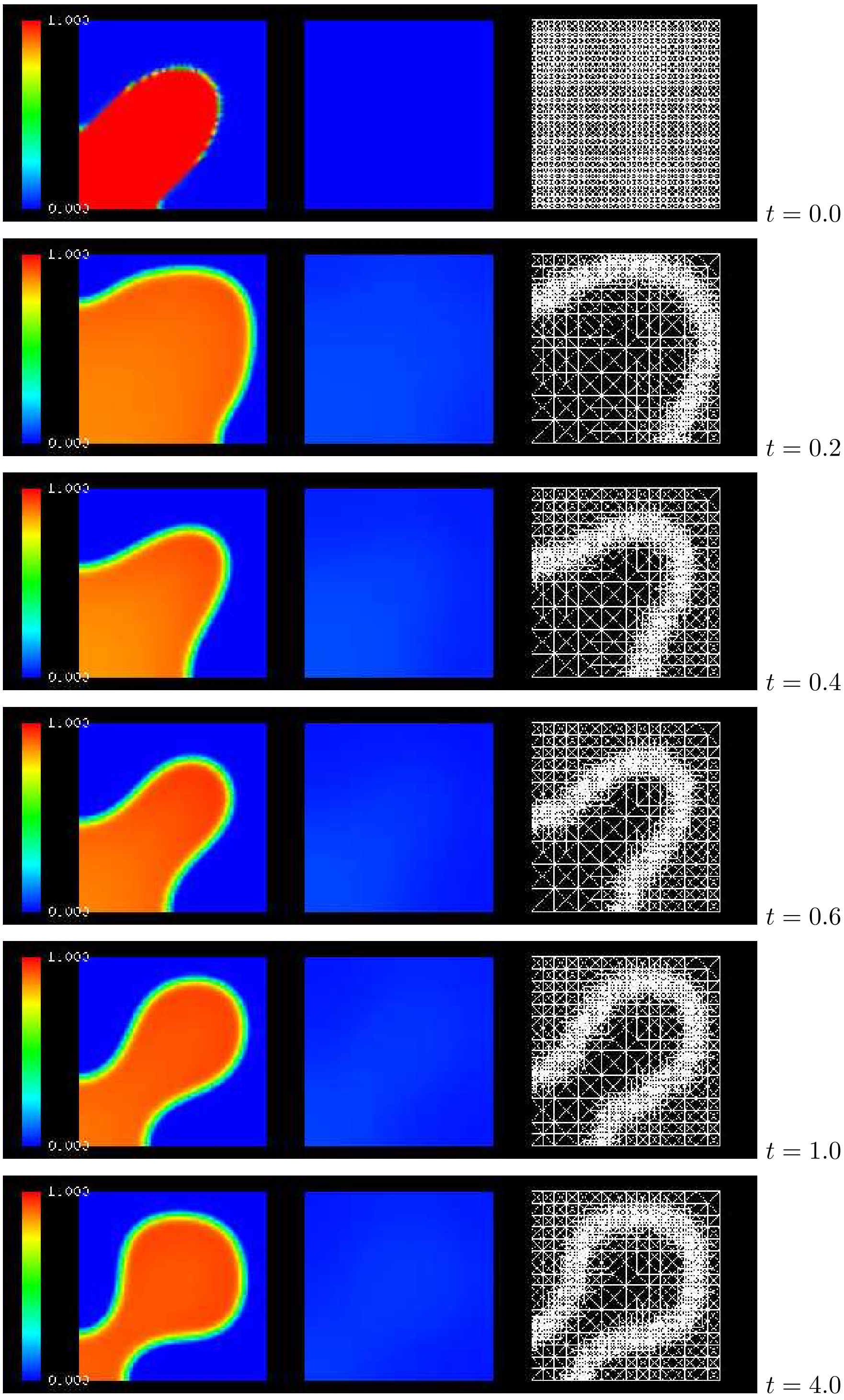

FIG. 2.1. *Snap shots of u, v and mesh from the numerical results of the activator-inhibitor system (*$\varepsilon = 0.01, \tau = 0.1, d = 1.0, a = 0.25, \lambda = 10.0$*)*

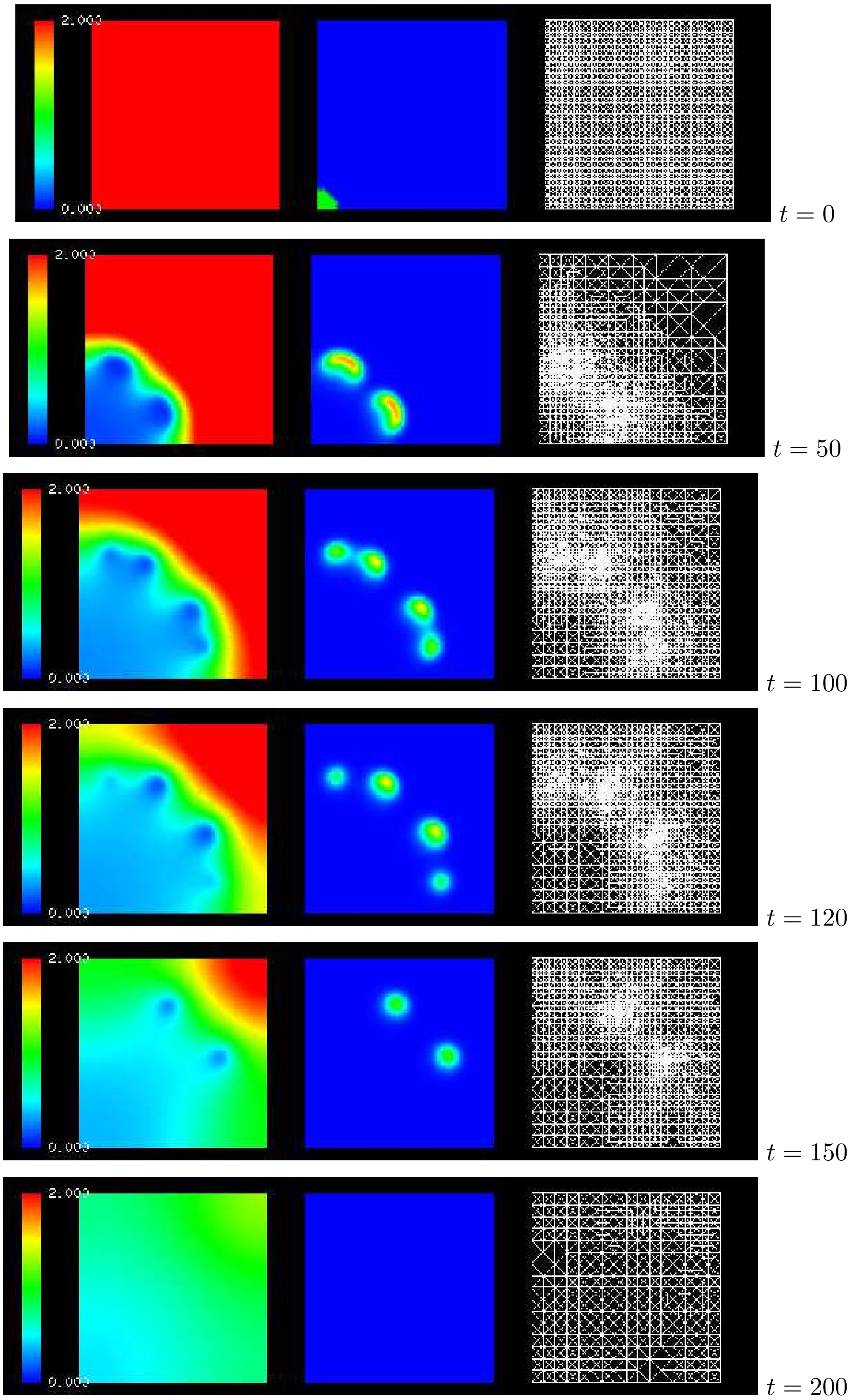

Fig. 2.2. *Snap shots of* u*,* v *and mesh from the numerical results of the Gray-Scott model* ($d_u = 11.5 \times 10^{-4}, d_v = 1.0 \times 10^{-4}, A = 0, \alpha = 0.25$)

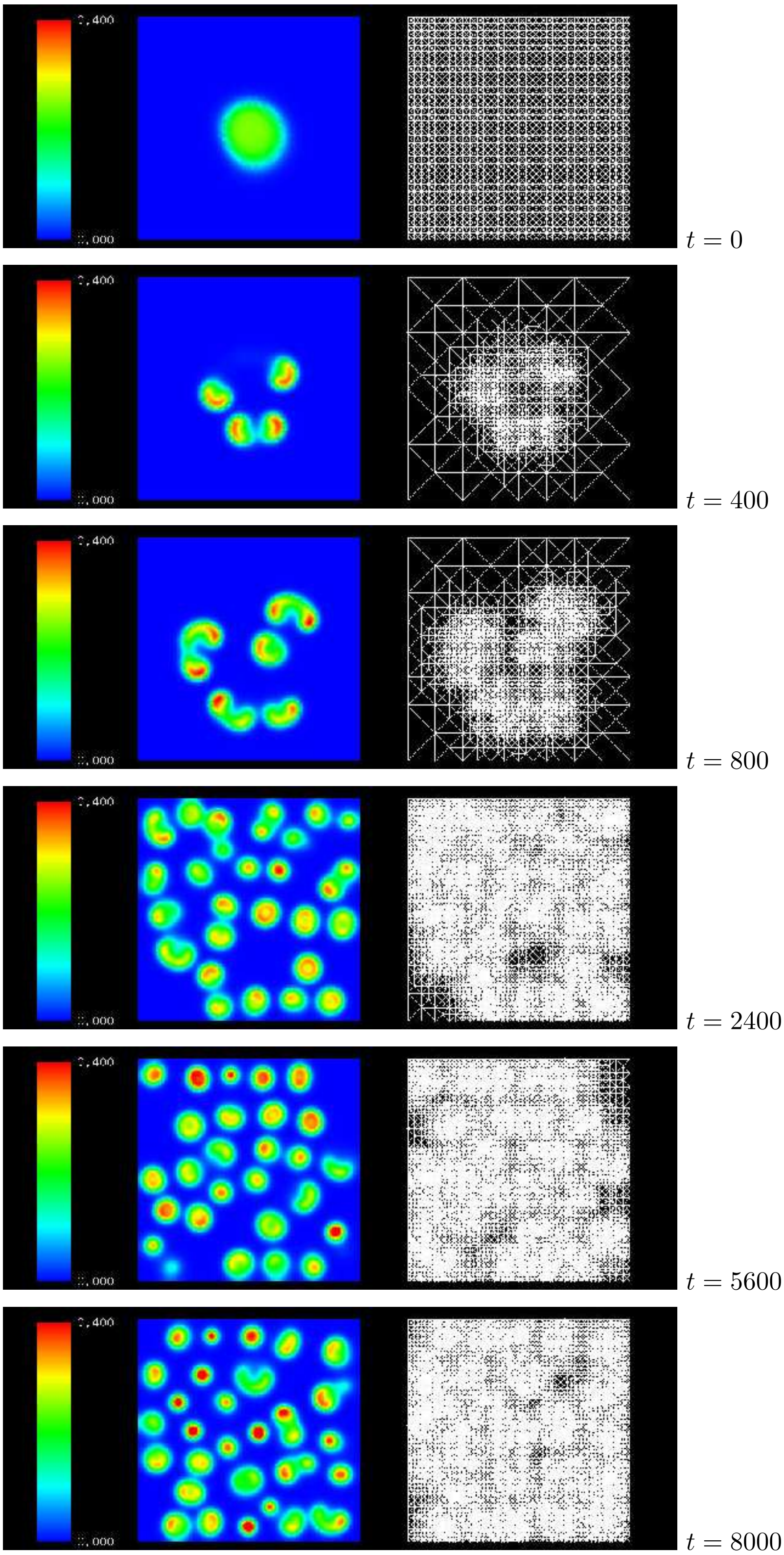

FIG. 2.3. *Snap shots of v and mesh from the numerical results of the Gray-Scott model ($d_u = 2.0 \times 10^{-5}, d_v = 10^{-5}, A = 0.02, \alpha = 0.077$)*

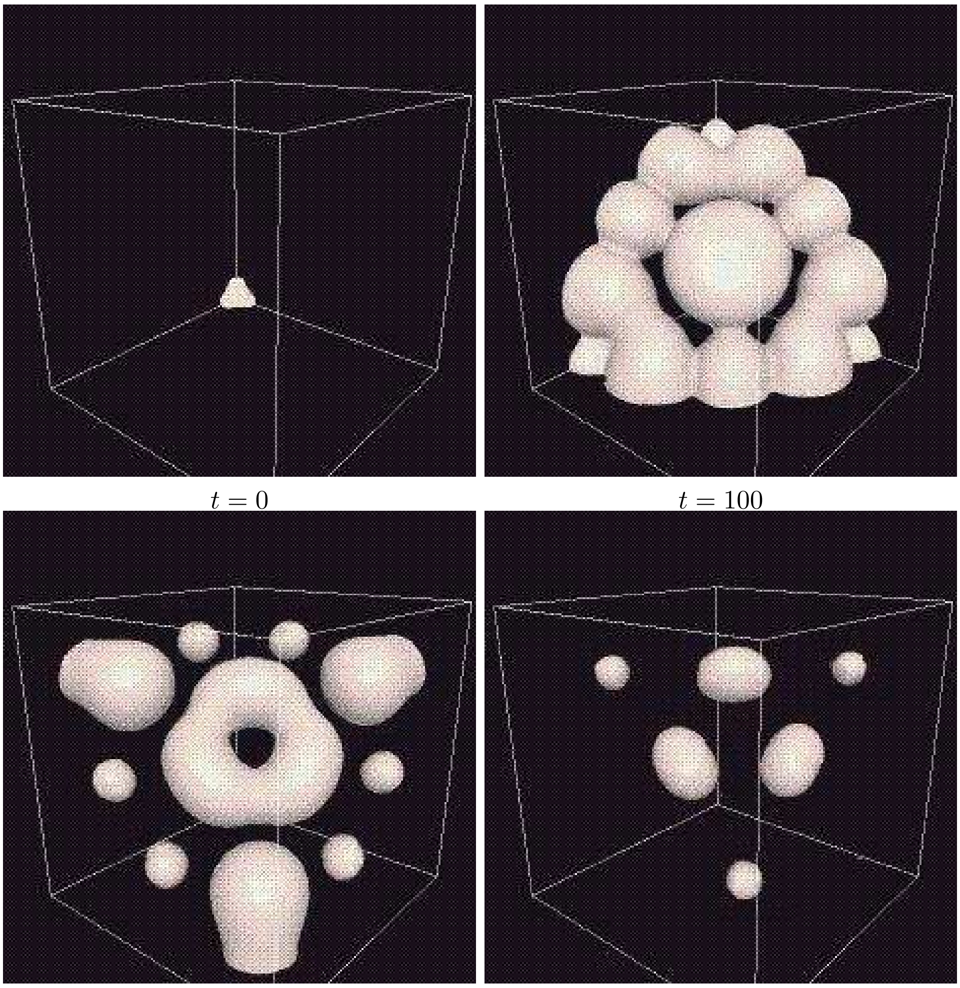

$t = 0$ $t = 100$

$t = 150$ $t = 200$

FIG. 2.4. *Snap shots of the isosurface ($v = 0.1$) of the numerical results of the three dimensional Gray-Scott model without supply ($d_u = 11.5 \times 10^{-4}$, $d_v = 1.0 \times 10^{-4}$, $A = 0$, $\alpha = 0.25$).*

of the Gray-Scott model without resource supply in Fig.2.4, and with resource supply in Fig.2.6 and Fig.2.8. In Fig.2.4, spots pattern appears and disappears and the total node number varries according to the disappearance of spots pattern similarly to Fig.2.2 (Fig.2.5(a)). The minimum mesh size, which is the shortest length of edge of the triangular element, is about $h = 7.8 \times 10^{-3}$ for $t < 170$ (Fig.2.5(b)). It corresponds to about 2.1×10^6 nodes in uniform mesh grid, if we use the mesh size h.

In the case of Gray-Scott model with resource supply (Fig.2.6, 2.8), the minimum mesh size varries only at early time stage, however, total node number varries as the pattern changes (Fig.2.7, 2.9). These are three dimensional self-replication processes.

We investigated a comparison of numerical accuracy between our adaptive mesh finite element method (AFEM) and the standard uniform mesh finite difference method (UFDM) in our previous paper. As a conclusion, we proposed the following empirical law: a numerical solution by AFEM with minimum mesh size h has almost same accuracy as a numerical solution by UFDM with uniform grid size h. The details of

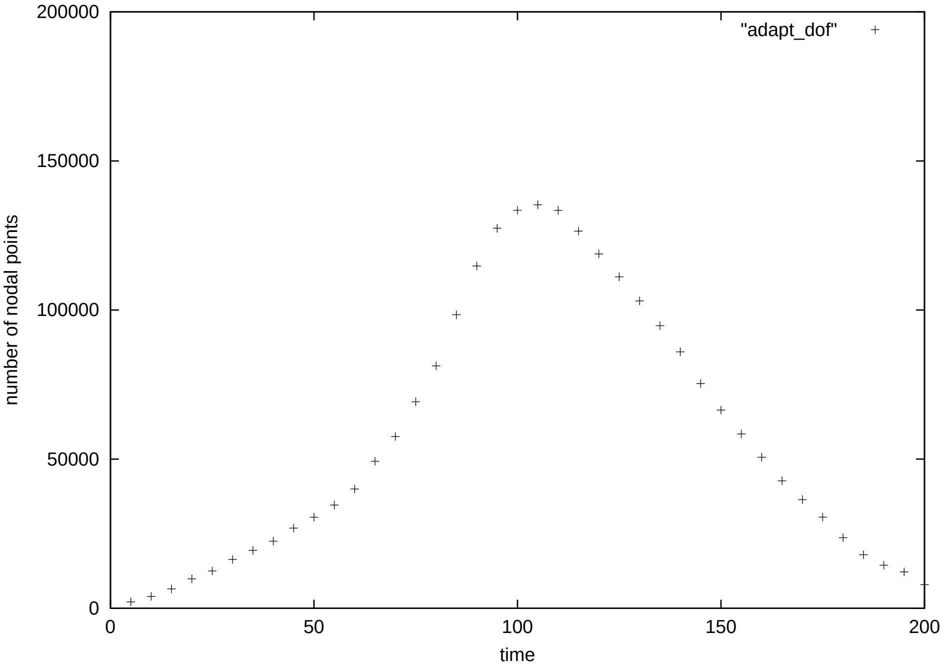

(a) Temporal change of total node number

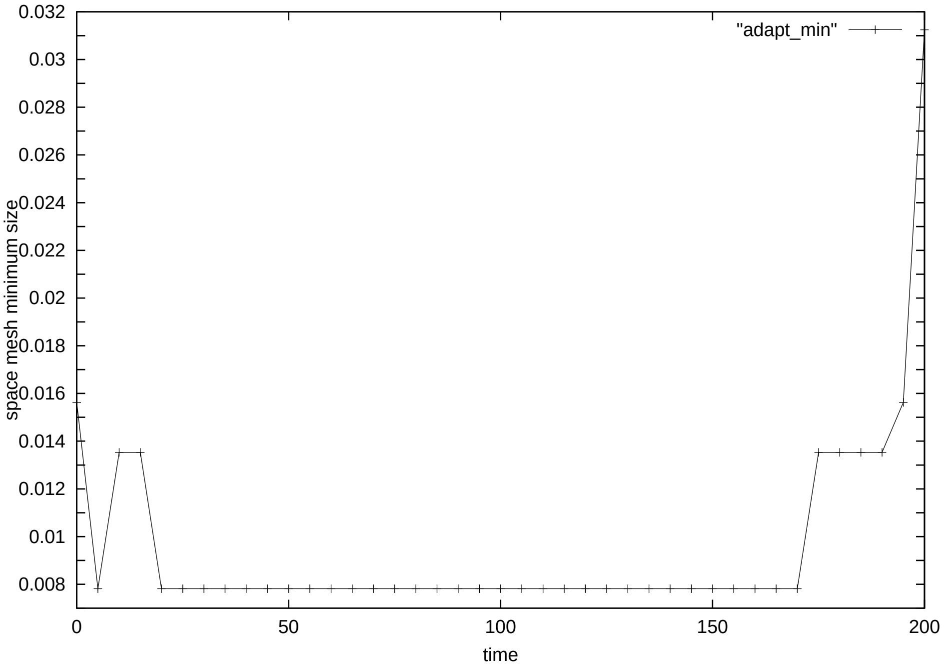

(b) Temporal change of minimum mesh size

Fig. 2.5. *Total mesh number and minimum mesh size in Fig.2.4.*

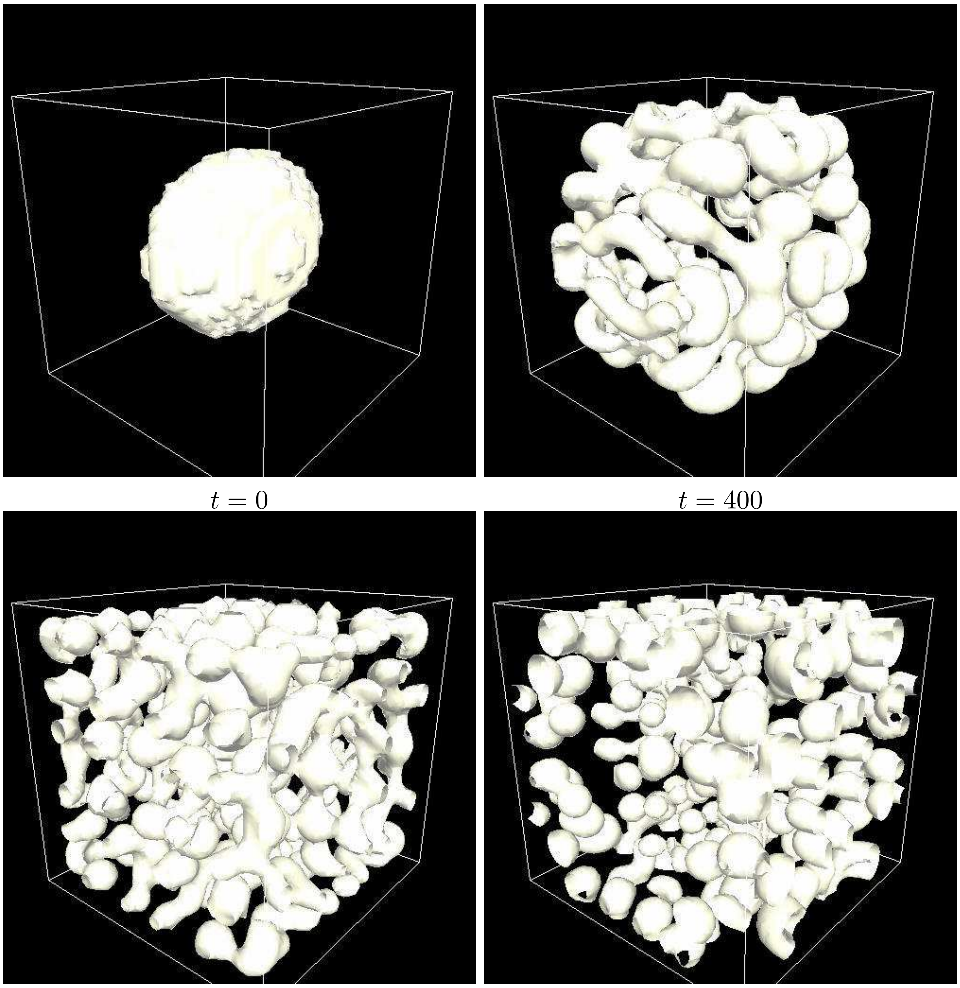

$t = 0$ $t = 400$

$t = 800$ $t = 4000$

FIG. 2.6. *Snap shots of the isosurface* ($v = 0.2$) *of the numerical results of the three dimensional Gray-Scott model* ($d_u = 2.0 \times 10^{-5}, d_v = 10^{-5}, A = 0.02, \alpha = 0.077$).

this discussion are given in [6].

To measure the effectiveness of the adaptive mesh FEM, we introduced a quantity for each adapted mesh with minimum mesh size h. For a triangular mesh $\mathcal{T}$, we define a quantity $C = C(\mathcal{T})$, which represents the compression rate of the number of the nodal points comparing with uniform grid of size h,

$$C := \frac{\text{Number of nodal points of AFEM}}{\text{Number of nodal points in UFDM of mesh size } h} \times 100 \quad (\%).$$

Since the minimum mesh size h and the number of nodal points of AFEM are changing in time, we use representative (average or maximum, etc.) values for them. We also remark that the number of nodal points in UFDM is roughly estimated by $|\Omega|/h^n$.

For spatially localized and sparse patterns, we expect that the adaptive mesh FEM works well and the compression rate C becomes small, from our intuitive idea. We show the compression rates on some typical examples of pattern dynamics problem

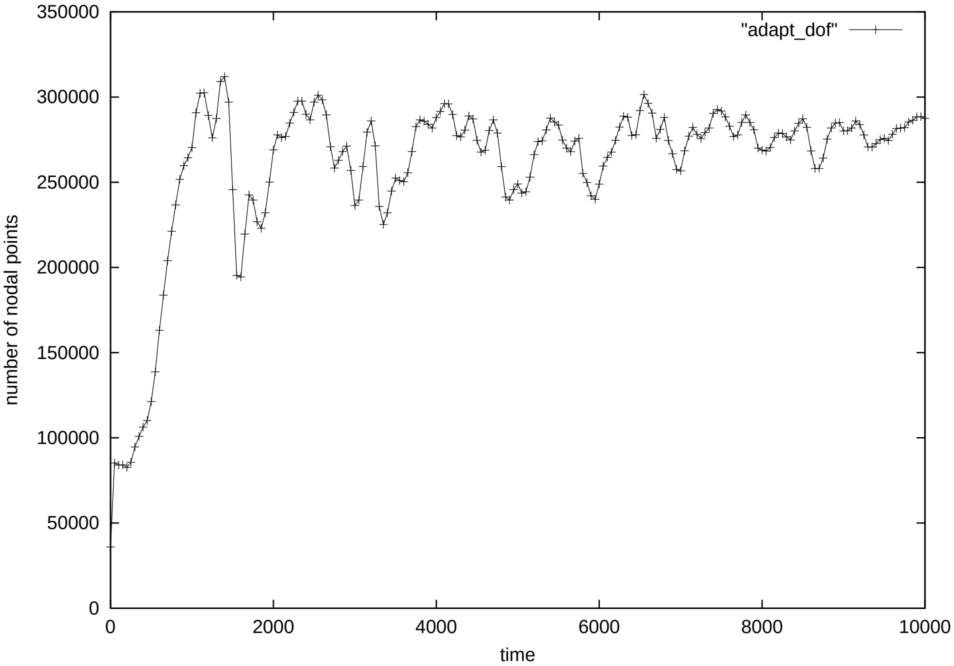

(a) Temporal change of total node number

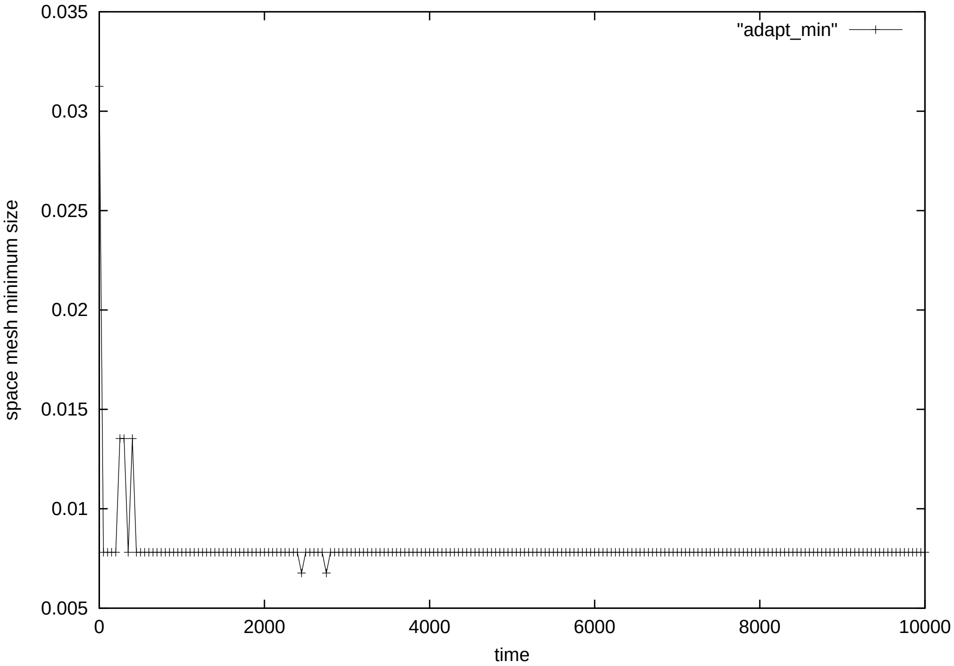

(b) Temporal change of minimum mesh size

Fig. 2.7. *Total mesh number and minimum mesh size in Fig.2.6.*

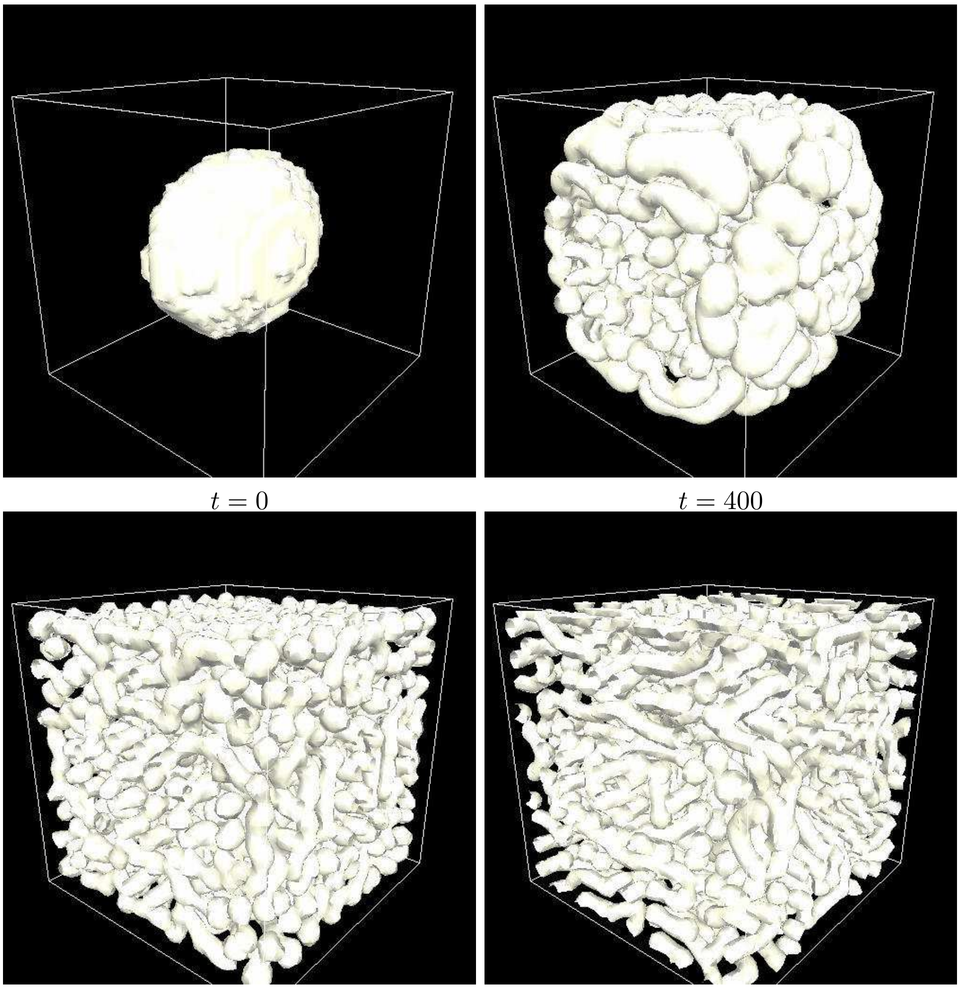

$t = 0$ $t = 400$

$t = 800$ $t = 4000$

FIG. 2.8. *Snap shots of the isosurface* ($v = 0.2$) *of the numerical results of the three dimensional Gray-Scott model* ($d_u = 2.5 \times 10^{-5}, d_v = 5.0 \times 10^{-6}, A = 0.02, \alpha = 0.077$).

by numerical results in Table 2.1.

Except for the case Fig.2.3 and Fig.2.8, the compression rates are sufficiently small and the adaptive mesh algorithm works very well. Even in the cases Fig.2.3 and Fig.2.8, the maximum value is relatively high (C=43%) but the average in time is smaller. We confirmed that adaptive FEM works well in some typical examples of pattern dynamics problems, even if the pattern looks very complicated and dense.

Comparing two and three dimensional simulations of the Gray-Scott model with same parameters (Fig.2.3 and Fig.2.6), we find very similar scale and structure of dense spot pattern in both cases. But we can observe that the compression rate in 3D case ($C \leq 14$ %) is much less than the 2D case ($C \leq 43$ %) from Table 2.1. This difference will be explained in section 4.

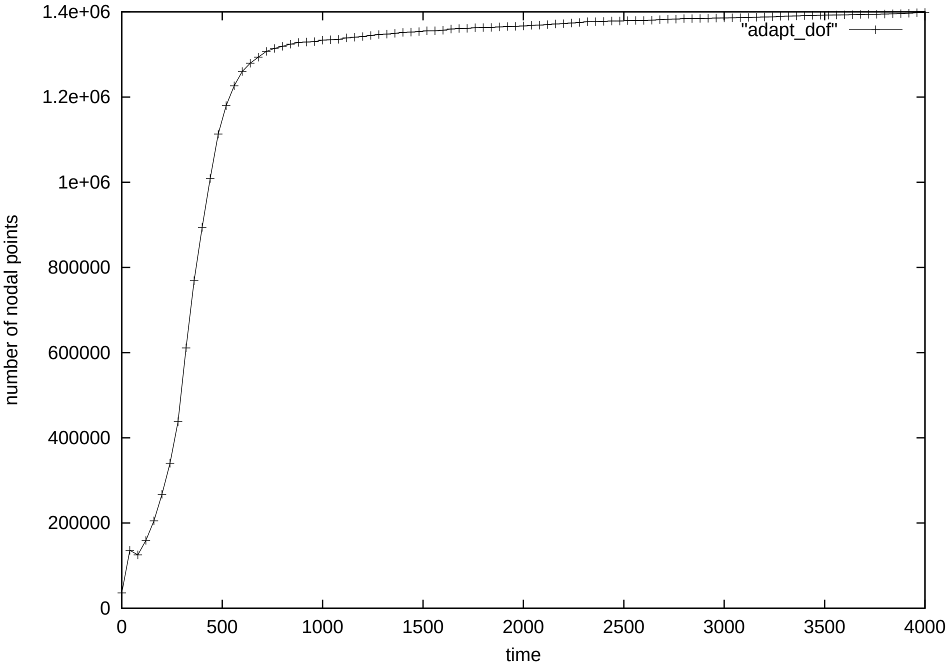

(a) Temporal change of total node number

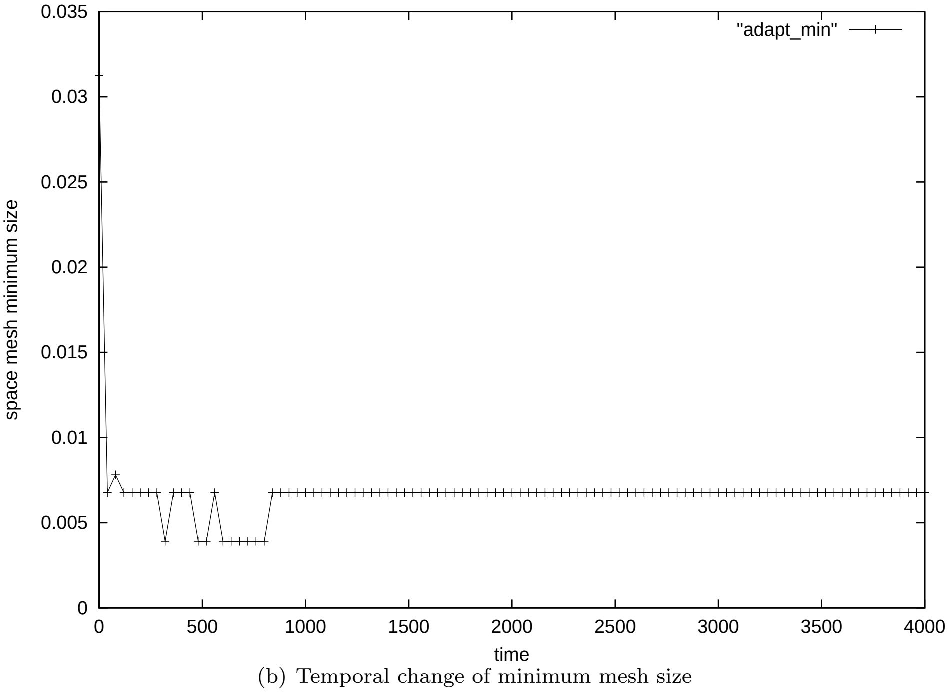

(b) Temporal change of minimum mesh size

FIG. 2.9. *Total mesh number and minimum mesh size in Fig.2.8.*

Table 2.1
Compression rates for pattern dynamics problems

		n	C
Activator-Inhibitor system	(Fig.2.1)	2	about 20%
Gray-Scott model without supply	(Fig.2.2)	2	$\leq 10\%$
Gray-Scott model with supply	(Fig.2.3)	2	$\leq 43\%$
Gray-Scott model without supply	(Fig.2.4)	3	$\leq 7\%$
Gray-Scott model with supply	(Fig.2.6)	3	$\leq 14\%$
Gray-Scott model with supply	(Fig.2.8)	3	$\leq 43\%$

3. Localization index.

In section 2, we have seen that the compression rate C is a good quantity which reflects usefulness of our adaptive mesh FEM. But the behavior of C is not so simple, and it is necessary to make it clear.

On the other hand, from numerical experiments for several pattern dynamics, the adaptive mesh looks well adapted to the profile of the numerical solution $u_h(t)$. In case that $u_h(t)$ has a localized pattern in a "small" region, the mesh becomes very fine only near the small region. For further quantitative study of these relations, we need to introduce a good index which represents a kind of spatial localization and complexity of the patterns.

We introduce the following quantity

$$L(u) := \frac{\int_\Omega |\nabla u| dx}{|\Omega| \ (\text{ess-sup}|\nabla u|)} \qquad (u \in W^{1,\infty}(\Omega),\ u \not\equiv \text{const.}).$$

This is a kind of normalized total variation of u with $0 < L(u) \leq 1$ and the following scale invariances. For arbitrary $a > 0$ and $b > 0$, we define $v(y) := bu(ay)$ for $y \in \Omega' = \{y \in \mathbb{R}^n;\ ay \in \Omega\}$. Then we have $L(v) = L(u)$. Moreover, if Ω is decomposed into N congruent subdomains as $\Omega = \cup_{j=1}^N \Omega_j$ and a function u defined on Ω has same profile on each Ω_j, then we have $L(u) = L(u_j)$ where $u_j := u|_{\Omega_j}$.

Since the "small" region of the spatially localized pattern is almost overlapped as the region where $|\nabla u|$ is large in many patterns, we can consider $L(u)$ to be a quantity which represents density of the pattern. In this sense, we call $L(u)$ *localization index of* u. If $L(u)$ is small, say $L(u) < 0.3$, u seems to exhibit a kind of patterns.

Table 3.1 shows the localization indexes of some typical functions in 1D, where $\Omega = (-l, l)$ for some $l > 0$. The case (i) and the cases (ii), (iii) correspond to internal layer of width $O(1/a)$ and to spike (spot) profiles of width $O(1/a)$, respectively, as $a \to \infty$. In these localized patterns, the localization indexes tend to zero as $a \to \infty$, more precisely, $L(u) = O(1/a)$.

On the other hand, a trigonometric function (iv) of wave length $O(1/a)$ has localization index $L(u) = 2/\pi \cong 0.64$, and its localization does not change as $a \to \infty$. We distinguish this kind of "uniform pattern" from the typical localized patterns appearing in reaction-diffusion systems.

In the case (v), we have $L(u) = 1$ for any $b \in \mathbb{R}$. We remark that $L(u) = 1$ if and only if u is a solution of the Eikonal equation:

$$|\nabla u| = \text{const.} \quad \text{a.e. in } \Omega.$$

In particular, all linear functions are solutions of Eikonal equation. In this case, there is no pattern of course, but the adapted mesh should be almost uniform and the compression rate is close to 100%.

TABLE 3.1

Localization index for each functions $u(x)$

	$u(x)$	$L(u)$	
(i)	$\tanh ax$	$\dfrac{\tanh al}{al}$	$a > 0$
(ii)	$\dfrac{1}{1+a^2x^2}$	$\dfrac{8al}{3\sqrt{3}(1+a^2l^2)}$	$a > 0$
(iii)	$e^{-a^2x^2}$	$\sqrt{\dfrac{e}{2}}\dfrac{1-e^{-a^2l^2}}{al}$	$a > 0$
(iv)	$\cos ax$	$\dfrac{2}{\pi}$	$a \neq 0,\ \dfrac{2al}{\pi} \in \mathbb{Z}$
(v)	$\lvert x-b\rvert$	1	$b \in \mathbb{R}$
(vi)	$\lvert x\rvert^{\alpha}$	$\dfrac{1}{\alpha}$	$\alpha \geq 1$

In the case (vi), $u(x)$ has boundary layers near $x = \pm l$ when $\alpha \to \infty$. The slope of the boundary layers is $|u'(\pm l)| = \alpha l^{\alpha-1}$ and it is quite large as $\alpha \to \infty$ if $l > 1$. But its localization index is $1/\alpha$.

For some typical patterns in multi-dimensional case, such as internal layer and spots pattern, their localization indexes will be calculated in the next section.

4. Localization index v.s. compression rate. We study the relation between the compression rate and the localization index through some numerical experiments. Let $\mathcal{T}(t)$ be the triangular finite element mesh at time t in our adaptive mesh FEM. Then the compression rate C at time t depends only on $\mathcal{T}(t)$: $C = C(\mathcal{T}(t))$.

But $\mathcal{T}(t_j)$ at j-th discrete time $t = t_j$ is determined from the previous mesh $\mathcal{T}(t_{j-1})$, the previous finite element solutions, the reaction-diffusion system under consideration including system parameters (e.g. ε in the activator-inhibitor system, etc.), and the choice of our finite element scheme including the adaptive mesh strategy. In the following, for simplicity, the finite element solution at time t are represented by $u_h(t)$, the reaction-diffusion system and its parameters are together represented by p, and the finite element scheme with adaptive mesh strategy is represented by the tolerance parameter *tol*. Then $\mathcal{T}(t_j)$ depends on $\mathcal{T}(t_{j-1})$, $u_h(t_{j-1})$, p, and *tol* in general, and its behavior seems to be very complicated. We remark that, in case of system, u_h represents the component which exhibits the pattern, e.g. the component u for (1.1) and the component v for (1.2).

The graph in Fig.4.1 exhibits $C(\mathcal{T}(t))$ in horizontal axis and $L(u_h(t))$ in vertical axis for the activator-inhibitor system (1.1) with $\tau = 0.1$,$d = 1.0$,$a = 0.25$, $\lambda = 10.0$, where ε changes as $\varepsilon = 0.009,\ 0.010,\ 0.012,\ 0.014,\ 0.016,\ 0.018,\ 0.020$, where a time sequence of $(C(\mathcal{T}(t_j)),\ L(u_h(t_j)))$ is plotted for each ε. Lines in the graph

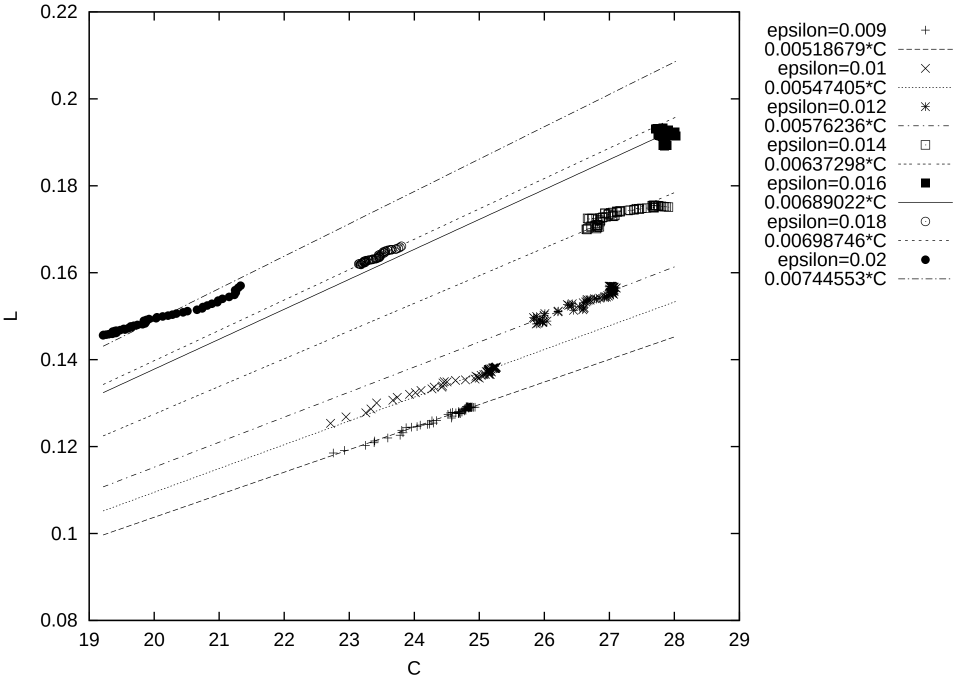

FIG. 4.1. *Compression rate v.s. localization index on the activator-inhibitor system*

are obtained by least squares fitting for each ε. Similarly, $(C(\mathcal{T}(t_j)),\ L(u_h(t_j)))$ for the Gray-Scott model without supply (Fig.2.2) are plotted in Fig.4.2(a) with a fitted line. In each case in Fig.4.1 and Fig.4.2(a), $(C(\mathcal{T}(t_j)),\ L(u_h(t_j)))$ are well fitted by a straight line through the origin.

In the case of the Gray-Scott model with supply (Fig.2.3) which is shown in Fig.4.2(b), $(C(\mathcal{T}(t_j)),\ L(u_h(t_j)))$ are not well fitted but roughly around a straight line.

To explain the above numerical results, let us consider a typical internal layer solution appearing in two dimensional reaction-diffusion systems with bistable nonlinearity, such as the activator-inhibitor system (Fig.2.1) and the Allen-Cahn equation ([5] etc.). Let $u_h(t)$ be a finite element solution with an internal layer $\Gamma(t)$, and let $|\Gamma(t)|$ be its length. Usually, a bistable system with fixed parameters p has its characteristic lengths, the height $H = H(p)$ and the width $\gamma = \gamma(p)$ of the internal layer (see Fig.4.3).

Since the total variation of $u_h(t)$ is close to $H|\Gamma(t)|$ and $\max|\nabla u_h(t)| \cong H/\gamma$ if $0 < \gamma << 1$, the localization index of $u_h(t)$ is roughly given by

$$L(u_h(t)) \cong \frac{H(p)|\Gamma(t)|}{|\Omega|H(p)/\gamma(p)} = \frac{\gamma(p)|\Gamma(t)|}{|\Omega|}.$$

On the other hand, an ideal finite element mesh $\mathcal{T}(t)$ for $u_h(t)$ should concentrate near the internal layer. Let $h(t)$ be the minimum mesh size of $\mathcal{T}(t)$. In the ideal case, a band region of width $\kappa\gamma$ covering $\Gamma(t)$ is divided into minimum size mesh and the other region is divided very sparsely. The coefficient κ represents the ratio of widths of $\Gamma(t)$ and the internal layer of the mesh $\mathcal{T}(t)$, and it is greater than 1 and roughly

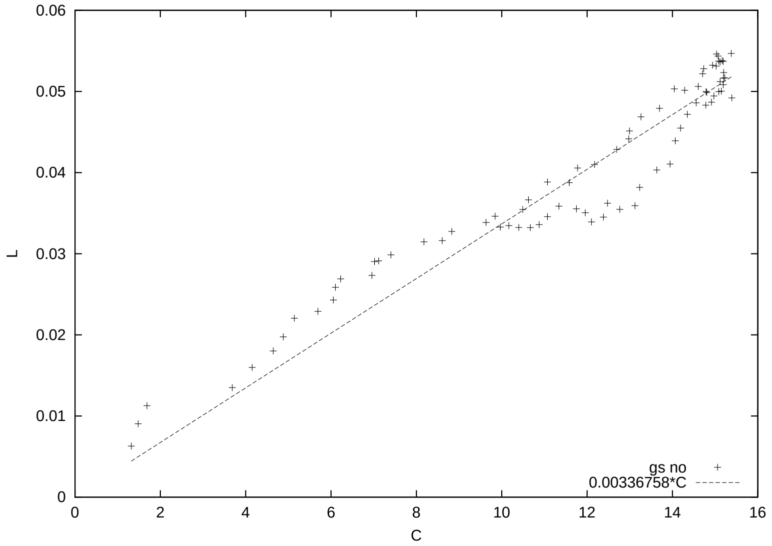

(a) The Gray-Scott model without supply ($A = 0$)

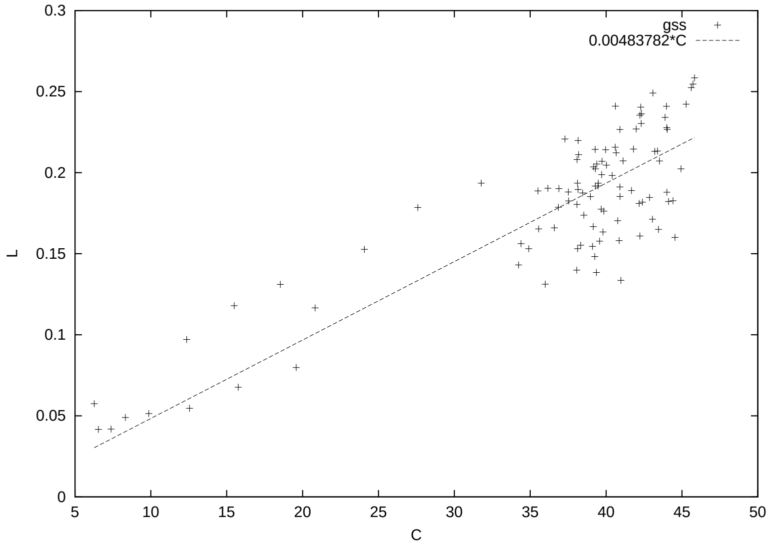

(b) The Gray-Scott model with supply ($A = 0.02$)

FIG. 4.2. *Compression rate v.s. localization index*

depends on the system parameters and the numerical scheme, i.e. $\kappa = \kappa(p, tol) > 1$ (see Fig.4.4). The compression rate of an ideal mesh is given by

$$C(\mathcal{T}(t)) \cong \frac{\kappa(p,tol)\gamma(p)|\Gamma(t)|/h(t)^2}{|\Omega|/h(t)^2} = \frac{\kappa(p,tol)\gamma(p)|\Gamma(t)|}{|\Omega|},$$

and, hence we have

$$C(\mathcal{T}(t)) \cong \kappa(p,tol)L(u_h(t)).$$

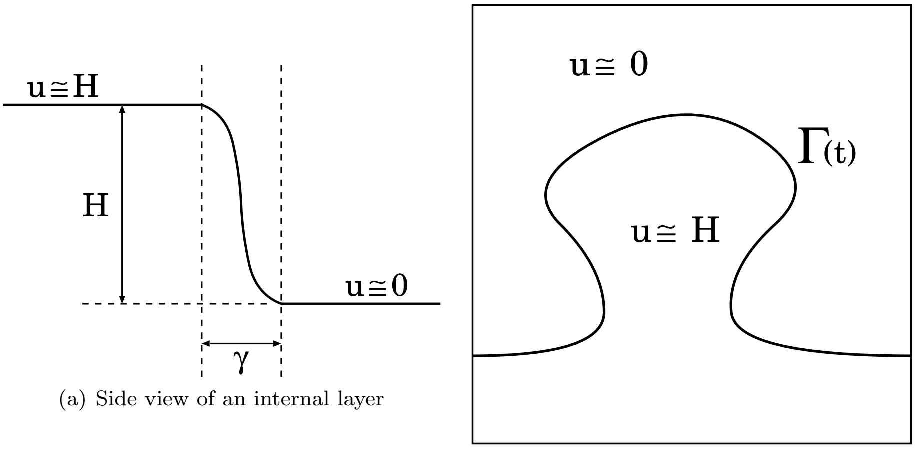

(a) Side view of an internal layer

(b) Top view of an internal layer

FIG. 4.3. *Profile of a typical internal layer*

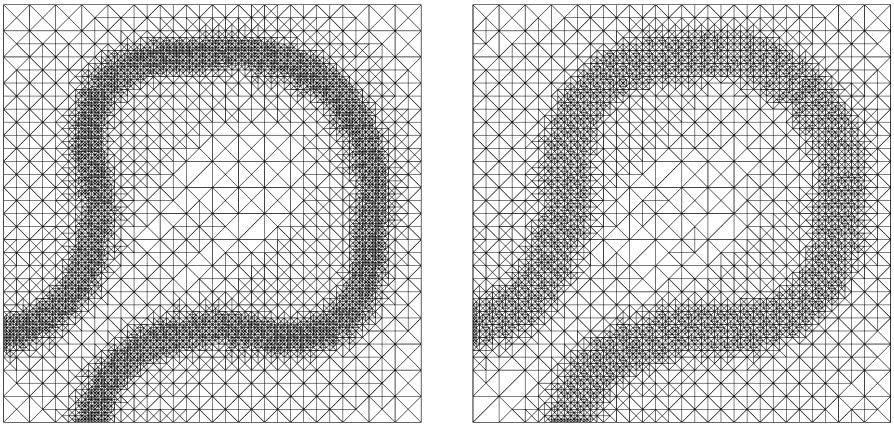

(a) $\varepsilon = 0.007$

(b) $\varepsilon = 0.009$

FIG. 4.4. *Typical mesh profile of eq.(1.1) at* $t = 4$

Next, let us consider a typical spots pattern of a multi-spike solution appearing in n dimensional reaction-diffusion systems, such as the Gray-Scott model and the Gierer-Meinhardt System ([9] etc.). Let $u_h(t)$ be a finite element solution with k spikes. We assume that the spike profile under consideration has its characteristic lengths, the height $H = H(p)$ and the radius of the spot $\rho = \rho(p)$ (see Fig.4.5), and that the spikes are distributed sufficiently far from each other.

Let a typical spike profile at the origin be denoted by $u_0(x)$. Since $\max |\nabla u_h(t)| \cong H/\rho$ and

$$\int_\Omega |\nabla u_h(t)| dx \cong k \int |\nabla u_0| dx \cong k \int_{B_n(\rho)} \frac{H}{\rho} dx = k \frac{H}{\rho} |B_n(\rho)|,$$

hold, where $B_n(\rho) := \{x \in \mathbb{R}^n;\ |x| < \rho\}$, the localization index of $u_h(t)$ is roughly

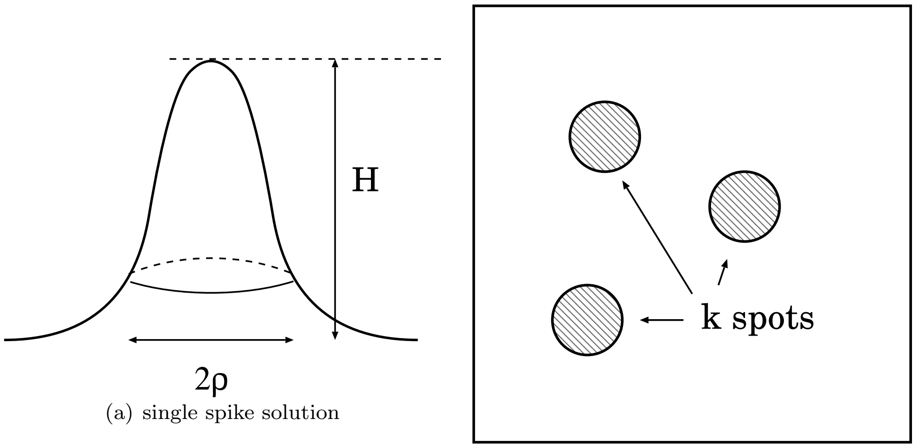

(a) single spike solution

(b) Spots pattern of k spikes solution

FIG. 4.5. *Profile of a typical spike solution*

given by

$$L(u_h(t)) \cong \frac{k(H(p)/\rho(p))|B_n(\rho(p))|}{|\Omega|H(p)/\rho(p)} = \frac{k|B_n(\rho(p))|}{|\Omega|}.$$

On the other hand, an ideal finite element mesh $\mathcal{T}(t)$ for $u_h(t)$ should concentrate near the spikes. Let $h(t)$ be the minimum mesh size of $\mathcal{T}(t)$. In the ideal case, a multi-spots region of radius $\mu\rho$ covering the k spots region is divided into minimum size mesh and the other region is divided very sparsely. The coefficient μ represents the ratio of radii of the support of a spike and the fine mesh spot region, and it is greater than 1 and roughly depends on the system parameters and the numerical scheme, i.e. $\mu = \mu(p, tol) > 1$. Hence, the compression rate of an ideal mesh is given by

$$C(\mathcal{T}(t)) \cong \frac{k|B_n(\mu(p,tol)\rho(p))|/h(t)^n}{|\Omega|/h(t)^n} \cong \mu(p,tol)^n L(u_h(t)). \tag{4.1}$$

In the both ideal cases, the compression rate $C(\mathcal{T}(t))$ is proportional to the localization index $L(u_h(t))$ and its proportionality constant depends only on p and tol. This explains the numerical experiments Fig.4.1, Fig.4.2(a) and Fig.4.2(b) well. In other words, it means that our adaptive mesh algorithm realizes almost ideal mesh adaptation in pattern dynamics problems.

As another application of the above analysis, we can explain the difference of compression rates of the Gray-Scott model with supply between two and three dimensional cases, which was mentioned at the end of section 2. This can be explained as a dimensional effect in terms of the localization index as follows.

Let $n \in \mathbb{N}$ be a spatial dimension. As a model of densely distributed spot patterns such as Fig.2.3 and Fig.2.6, we suppose a periodic structure of a box cell which contains a single spot. Let $\rho > 0$ and $H > 0$ be a typical radius and a typical height of a spike, respectively, and let $l > \rho$ be a half of a typical distance between centers of two nearest spots. We suppose that the size of domain Ω is enough larger than the cell size $2l$.

We consider a box cell

$$Q_n(l) := \{x = (x_1, \cdots, x_n) \in \mathbb{R}^n;\ |x_i| < l \ \ (i = 1, \cdots, n)\},$$

of size $2l$ and a function

$$u(x) = \max\left\{H\left(1 - \frac{|x|}{\rho}\right),\ 0\right\} \qquad (x \in Q_n(l)).$$

This is a simplified profile of the single spike solution shown in Fig.4.5(a).

The dense spot patterns in Fig.2.3 and Fig.2.6 are modeled by setting the box cell $Q_n(l)$ periodically in each x_i-direction with a period $2l$. The function $u(x)$ is extended to whole domain periodically, too. The number of spots in Ω is approximately equal to $|\Omega|/|Q_n(l)|$.

Let $L_n := L(u)$ be the localization index of u in n dimensional case. Then, since $|\nabla u(x)| = H/\rho$ for a. e. $x \in B_n(\rho)$, we have

$$L_n = \frac{\int_\Omega |\nabla u(x)|dx}{|\Omega|\frac{H}{\rho}} \cong \frac{\frac{|\Omega|}{|Q_n(l)|}\int_{B_n(\rho)} \frac{H}{\rho}dx}{|\Omega|\frac{H}{\rho}} = \frac{|B_n(\rho)|}{|Q_n(l)|} = \left(\frac{\rho}{2l}\right)^n |B_n(1)|.$$

From the previous result (4.1), the ideal compression rate in n dimensional case is given by $C_n = \mu^n L_n$. It is a natural assumption that the coefficient μ does not depend on n and satisfies $\rho < \mu\rho < l$. As a consequence, the ratio of C_2 and C_3 (in Table 2.1, it is $C_3/C_2 \cong 14/43 \cong 1/3$) is estimated as

$$\frac{C_3}{C_2} \cong \frac{\mu\rho|B_3(1)|}{2l|B_2(1)|} = \frac{\frac{4\pi}{3}\mu\rho}{2\pi l} = \frac{2\mu\rho}{3l} < \frac{2}{3}. \tag{4.2}$$

In stead of the above periodic structure, we can assume the closest-packed structure in two or three dimension. In two dimension, the centers of spots are placed on all node of a triangular grid tiled with copies of an equilateral triangle with edge size $2l$. In three dimension, the face-centered cubic lattice structure (FCC) or the hexagonal closest-packed structure (HCP) is assumed. Since their packing densities are $\pi/(2\sqrt{3})$ for $n = 2$ and $\pi/(3\sqrt{2})$ for $n = 3$, the estimate (4.2) becomes

$$\frac{C_3}{C_2} \cong \frac{\mu\rho}{l}\sqrt{\frac{2}{3}} < \sqrt{\frac{2}{3}}.$$

From this estimate, we can expect a dimensional effect by which the adaptive mesh FEM works more effectively in 3D than 2D. The results in Table 2.1 support that our adaptive scheme realizes this dimensional effect.

5. Application and concluding remarks.

We have presented a quantitative study of efficiency of an adaptive mesh finite element method for several reaction-diffusion systems which produce various kind of spatiotemporal patterns in 2D and 3D. Through several numerical examples and analysis, it was shown that our adaptive mesh algorithm works well for spatially localized pattern dynamics. We believe that the adaptive mesh simulation becomes a more important and indispensable tool in the analysis of spatiotemporal pattern dynamics. As such an example, here we show a small application of our method to a reaction-diffusion system.

In the simulation shown in Fig.2.2, several spots appear in the variable v and expand from the lower left corner with splitting, where initial conditions are radially symmetric except for the domain shape. The minimum mesh size is about $h = 8.0 \times 10^{-3}$ and it seems to be sufficiently small. But the radial symmetry is broken in Fig.2.2 numerically. Is this an influence from the boundary which is not radially symmetric?

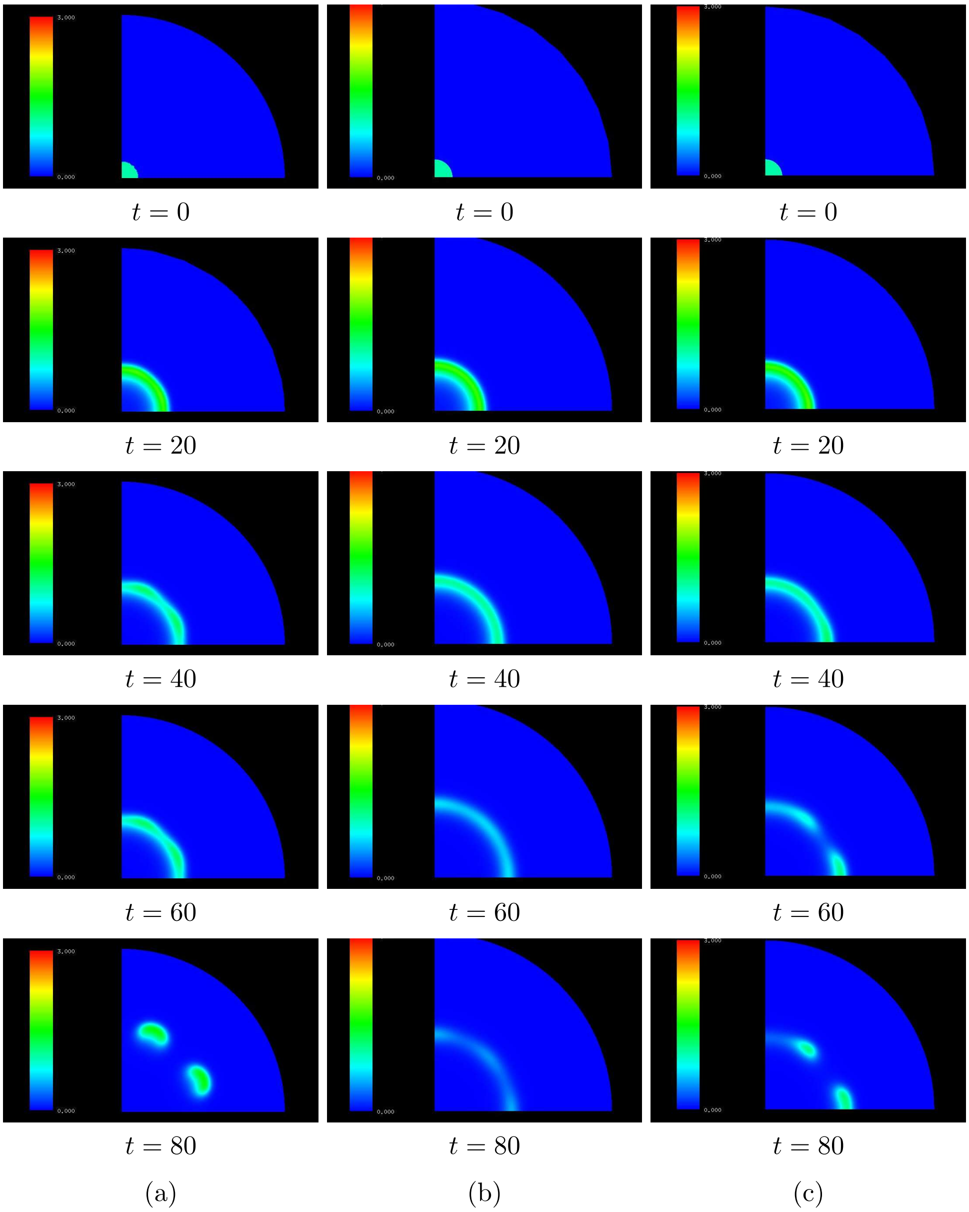

FIG. 5.1. *Unstable expanding ring pattern in the Gray-Scott model where (a)* $h = 2.0 \times 10^{-3}$, *(b)* $h = 2.0 \times 10^{-4}$, *(c)* $h = 2.0 \times 10^{-4}$ *with small perturbation.*

To remove the influence from the radial asymmetry of domain shape, we consider a quarter of a disk: $\Omega = \{x = (x_1, x_2) \in \mathbb{R}^2;\ |x| < 1,\ x_1 > 0,\ x_2 > 0\}$, with the following same initial condition;

$$\left\{ \begin{array}{lcl} u_0(x) & = & u_0 > 0 \quad (\text{const.}) \\ & & \\ v_0(x) & = & \left\{ \begin{array}{ll} 1 & (\ |x| \leq 0.1\ ) \\ 0 & (\ \text{otherwise}\ ), \end{array} \right. \end{array} \right. \tag{5.1}$$

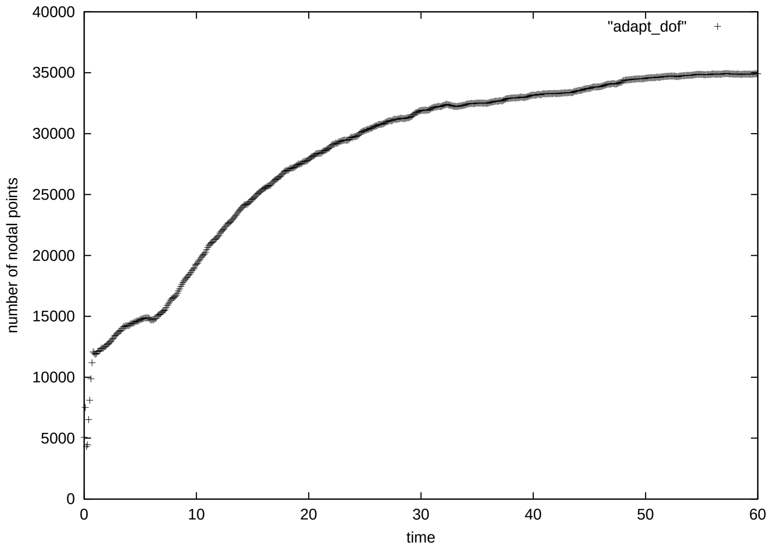

FIG. 5.2. *Temporal change of number of nodal points in Fig.5.1 (b).*

and with parameters given in Fig.2.2. Then, from the uniqueness of the solution of the reaction-diffusion system, it is clear that the exact solution has to be radially symmetric.

A numerical result with a tiny minimum mesh size $h = 2.0 \times 10^{-3}$ is shown in Fig.5.1 (a). A radial ring pattern expands in the beginning, but it is destabilized around $t = 40 \sim 60$ and splits into two spots contrary to the radially symmetric exact solution. Comparing with Fig.2.2, the radially symmetric pattern is more stable and the split occurs later. This computation suggests that the radially symmetric exact solution is not stable, and the source of breaking the ring pattern seems to be the anisotropy of the mesh.

Simulations shown in (b) and (c) of Fig.5.1 are computed with smaller tolerance and the minimum mesh size is about $h = 2.0 \times 10^{-4}$ during the computation in both cases, where we add small perturbation to the initial condition only in simulation (c). In (b), the numerical solution keeps an almost radially symmetric ring pattern which is expanding and fading out in time. On the other hand, the ring pattern splits in (c) because of an influence of the perturbation.

The temporal evolution of total node number in simulation (b) is shown in Fig.5.2. The maximum number of nodes is about 35000. In this case, the compression rate is less than 0.18 since the computational domain is much larger than the region occupied by the pattern. Since the ring dissapears around $|x| = \frac{1}{2}$, it may be possible to compute it on the half size domain. But the compression rate is still less than $0.18 \times 2^2 = 0.72$ even in the half size domain.

If we want to study a behavior of such unstable exact solution through numerical simulation, very fine mesh size like $h = 2.0 \times 10^{-4}$ is required as we have seen above. It is usually very difficult to realize such tiny mesh without adaptive mesh method.

The behavior of the compression rate of mesh, which is a good index for mesh adaptivity, is well explained by the localization index. The localization index of a numerical solution, which is a quantity introduced in this paper, characterizes localization of a pattern exhibited by the numerical solution.

In this paper and our previous one [6], we have attempted to study mesh adaptivity and pattern profiles quantitatively. Their quantitative characterizations have been established to a certain extent in terms of the compression rate and the localization index. In the field of pattern dynamics and its numerical simulation, we expect that these quantities will become standard tools and that this study becomes a step toward future more intensive analysis.

Acknowledgment. The authors express appreciation to the creators of ALBERTA; Dr. Alfred Schmidt and Dr. Kunibert G. Siebert, and to Dr. Michael Fried who is one of the first users of ALBERTA, for their kind help in the beginning of our use of the beautiful numerical toolbox ALBERTA. The authors also thanks to the creators of visual presentation software, GRAPE, which was developed in the University of Bonn. GRAPE was used to create some figures in this paper. The first author was partly supported by the project "Jindřich-Nečas Center for Mathematical Modelling" LC06052 of the Ministry of Education, Youth and Sport of the Czech Republic.

REFERENCES

[1] E. Bänsch, *An Adaptive Finite-element Strategy for the Three-dimensional Time-dependent Navier-Stokes Equations*, J. Comput. Appl. Math. **36** (1991) 3–28.

[2] S.C. Brenner and C. Carstensen, Finite Element Methods, in: E. Stein et al. (Ed.), *Encyclopedia of Computational Mechanics Vol.1*, Chapter 4., John Wiley & Sons, Ltd., 2004, pp.73–118.

[3] M.E. Cawood, V.J. Ervin, W.J. Layton, and J.M. Maubach, *Adaptive Defect Correction Methods for Convection Dominated, Convection Diffusion Problems*, J. Comput. Appl. Math. **116** (2000) 1–21.

[4] Z. Chen, R.H. Nochetto, and A. Schmidt, *Error Control and Adaptivity for a Phase Relaxation Model*, M2AN Math. Model. Numer. Anal. **34** (2000) 775–797.

[5] P.C. Fife, *Dynamics of Internal Layers and Diffusive Interfaces*, CBMS-NSF Regional Conference Series in Applied Mathematics **53**. SIAM, Philadelphia, PA (1988).

[6] M. Kimura, H. Komura, M. Mimura, H. Miyoshi, T. Takaishi, and D. Ueyama, Adaptive Mesh Finite Element Method for Pattern Dynamics in Reaction-Diffusion Systems, in: Proc. of the Czech-Japanese Seminar in Applied Mathematics 2005, COE Lecture Note Vol.3, Faculty of Mathematics, Kyushu University ISSN 1881-4042, 2006, pp.56-68. http://www.math.kyushu-u.ac.jp/coe/

[7] H. Komura, On Adaptive Mesh Finite Element Methods – Application of ALBERT –, Master's thesis, Graduate School of Science, Hiroshima University, 2002 (in Japanese).

[8] K.J. Lee, W.D. McCormick, Q. Ouyang, and H.L. Swinney, Pattern Formation by Interacting Chemical Fronts, Science **261** (1993), 192–194.

[9] H. Meinhardt, and A. Gierer, *Applications of a Theory of Biological Pattern Formation Based on Lateral Inhibition*, J. Cell Sci. **15** (1974) 321–346.

[10] M. Mimura, *Pattern Formation in Consumer-Finite Resource Reaction-diffusion systems*, Publ. Res. Inst. Math. Sci. **40** (2004) 1413–1431.

[11] W. F. Mitchell, Adaptive Refinement for Arbitrary Finite-Element Spaces with Hierarchical Bases, J. Comput. Appl. Math. **36** (1991) 65–78.

[12] H. Miyoshi, *The Validity of an Adaptive Mesh Finite Element Method for Reaction-Diffusion Systems – Quantitative Analysis of Localized Patterns –*, Master's thesis, Graduate School of Science, Hiroshima University, 2003 (in Japanese).

[13] J.D. Murray, *Mathematical Biology*, Springer-Verlag (1989).

[14] Y. Nishiura, and D. Ueyama, *A Skeleton Structure of Self-replicating Dynamics*, Physica D **130** (1999) 73–104.

[15] Y. Nishiura, and D. Ueyama, *Spatio-Temporal Chaos for the Gray-Scott Model*, Physica D **150** (2001) 137–162.

[16] J. E. Pearson, *Complex Patterns in a Simple System*, Science **261** (1993) 189–192.

[17] R. Rannacher, *Adaptive Galerkin Finite Element Methods for Partial Differential Equations*, J. Comput. Appl. Math. **128** (2001) 205–233.

[18] C. Rocşoreanu, A. Georgescu, and N. Giurgiţeanu, *The FitzHugh-Nagumo Model, Bifurcation and Dynamics*, Kluwer academic publishers, Dordrecht (2000).

[19] A. Schmidt, *Approximation of Crystalline Dendrite Growth in Two Space Dimensions*, Acta Math. Univ. Comenian. (N.S.) **67** (1998) 57–68.

[20] A. Schmidt, and K. G. Siebert, *An Adaptive Hierarchical Finite Element Toolbox, Version: ALBERT-1.0*, Freiburg University, 2000.

[21] A. Schmidt, and K. G. Siebert, *Design of Adaptive Finite Element Software. The Finite Element Toolbox ALBERTA*, Lecture Notes in Computational Science and Engineering, 42. Springer-Verlag, Berlin (2005).

[22] T. Takaishi, M. Mimura, and Y. Nishiura, *Pattern Formation in Coupled Reaction-Diffusion Systems*, Japan J. Indust. Appl. Math. **12** (1995) 385–424.

[23] D. Ueyama, *Dynamics of Self-Replicating Patterns in the One-Dimensional Gray-Scott Model*, Hokkaido Math. J. **28** (1999), 175–210.

[24] D. Ueyama, *Tree-Branch Patterns that Appear in Reaction-Diffusion Systems*, in : Reaction-Diffusion Systems: Experiments and Theoretical Models in Biology and Chemistry (Kyoto, 2000), Surikaisekikenkyusho Kokyuroku **1167**, 2000, pp.73–74 (in Japanese).

[25] R. Verfürth, *A Posteriori Error Estimates for Nonlinear Problems. Finite Element Discretizations of Elliptic Equations*, Math. Comp. **62** (1994) 445–475.

[26] A.T. Winfree, *The Geometry of Biological Time, Second ed.,* Interdisciplinary Applied Mathematics **12**, Springer-Verlag, New York (2001).

[27] P.A. Zegeling, and H.P. Kok, *Adaptive Moving Mesh Computations for Reaction-diffusion Systems*, J. Comput. Appl. Math. **168** (2004) 519–528.